

# Topological phonons and Weyl lines in 3 dimensions

Olaf Stenull, C. L. Kane, and T. C. Lubensky

*Department of Physics and Astronomy, University of Pennsylvania, Philadelphia, PA 19104, USA*

(Dated: June 2, 2016)

Topological mechanics and phononics have recently emerged as an exciting field of study. Here we introduce and study generalizations of the three-dimensional pyrochlore lattice that have topologically protected edge states and Weyl lines in their bulk phonon spectra, which lead to zero surface modes that flip from one edge to the opposite as a function of surface wavenumber.

PACS numbers: 62.20.D-, 03.65.Vf

Mechanical lattices with a perfect balance between the number of degrees of freedom and the number of constraints (springs) with unit cells of appropriate internal geometry exhibit zero-frequency modes at boundaries even though they have very few if any zero modes in their bulk [1, 2]. The topological origin of these zero modes was explained in Ref. [3], which introduced the framework for a phononic version of topological band theory that is well known in electronic contexts, including polyacetylene [4], quantum Hall systems [5, 6], and topological insulators [7–12]. So far, attention has focused on one- [13] and two-dimensional (2d) [14–17] model systems, such as the generalized kagome lattice (GKL) introduced in Ref. [3], which places masses and central-force springs on a lattice of corner-sharing triangles. In this paper, we consider the natural three-dimensional (3d) generalization of this system – a generalized pyrochlore lattice (GPL) with deformed corner sharing tetrahedra, whose edges are occupied by central-force springs, as depicted in Fig. 1. We show that the bulk phonon spectrum of these lattices exhibit lines of topologically protected zero modes, analogous to lines of touching bands in line-node semimetals [18–21] and gyroid photonic crystals [22], that cause the number of protected surface modes to undergo discontinuous jumps as a function of surface wavenumber.

In 2d GKLs, there exist classes of conformations in which all of the bulk vibrational modes, except for the zero-wavevector acoustic modes, have a finite frequency. These fully “gapped” systems fall into topological classes distinguished by topological invariants characterizing their reciprocal-space band structure. Topological zero-frequency edge modes arise from an interplay between this bulk topological structure and the local mismatch in the number of degrees of freedom and constraints, so that given the bulk topological invariants and the local structure of the surface termination, it is possible to predict the number of zero-frequency modes localized at a surface. In GKLs, the transition between topologically distinct phases is marked by the existence of a line in the Brillouin zone along which normal-mode frequencies vanishes. This line of zero modes is a consequence of the existence of straight lines of bonds, which we call straight filaments, that carry a state of self stress

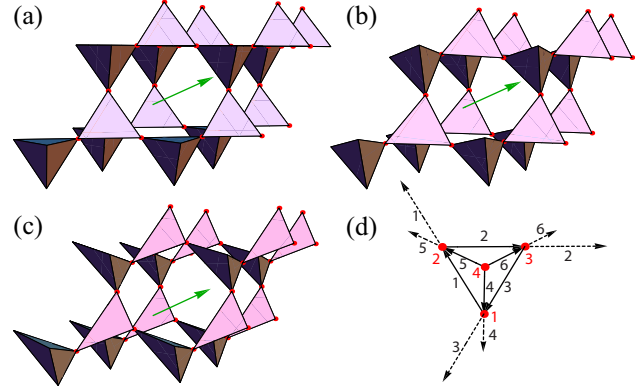


FIG. 1. (Color Online) (a) The original pyrochlore lattice and the GPL in the (b)  $X_1$  and (c)  $X_{-1}$  conformations (see text). The (green) arrow represents the  $(1, 1, 1)$ -direction. (d) The unit cell of (a). The (red) dots with the (red) numbers mark the basis sites. The solid (dashed) arrows designate the bond vectors  $\mathbf{a}_b$  ( $\mathbf{a}'_b$ ) of the internal (external) bonds.

(SSS) in which the bonds are under tension but site forces vanish. The Maxwell-Calladine counting rule (see below) [23, 24] applied with periodic boundary conditions, then guarantees corresponding zero modes.

Three-dimensional GPLs have a richer structure than two-dimensional GKLs. We find that, like GKLs, they exhibit gapless bulk modes associated with localized SSSs: Arrays of parallel lines of SSSs (straight filaments) – four in the undistorted pyrochlore lattice aligned along the tetrahedral edges – have associated planes of zero modes in reciprocal space aligned perpendicular to the array filaments, and flat planes of self-stress have associated perpendicularly aligned lines of zero modes in reciprocal space. As in the GKL, the bulk zero modes on these planes (lines) can be lifted to non-zero frequency by distorting the lattice to remove the straight lines (flat planes) of bonds. However, a new phenomenon, which did not occur in the GKL, arises. There are lines of bulk zero modes in reciprocal space that are protected by an integer topological invariant defined on a path that encircles them. These are the analog of Weyl lines that exist in electronic [18–21] and photonic [22] systems. Analogous Weyl/Dirac points [19, 25, 26] can also be present

in  $2d$ , as in the electronic spectra of graphene [27–29] and phonon spectra in deformed square lattices [16] and  $2d$  models of jammed matter [17], and they appear to be generic in large-unit-cell Maxwell lattices. We will show that the presence of Weyl lines in the bulk also has important consequences for the number and location of surface zero modes.

Our GPL is based on the usual pyrochlore lattice with 4-site, 12-bond unit cells. We choose our standard reference unit cell to have sites at the 4 corners of a tetrahedron at the basis positions  $\mathbf{r}_1 = \frac{1}{2}(1, 1, 0)$ ,  $\mathbf{r}_2 = \frac{1}{2}(0, 1, 1)$ ,  $\mathbf{r}_3 = \frac{1}{2}(1, 0, 1)$ , and  $\mathbf{r}_4 = (0, 0, 0)$  and bonds as shown in Fig. 1 (d). Note that this cell lacks inversion symmetry, as do all other unit cells in GPLs, and, as a result, it has a nonvanishing dipole moment when charges  $d = +3$  are placed at its sites and charges  $-1$  at the center of its bonds. The primitive translation vectors of the lattice are  $\mathbf{T}_1 = (1, 1, 0)$ ,  $\mathbf{T}_2 = (0, 1, 1)$  and  $\mathbf{T}_3 = (1, 0, 1)$ . There are six internal bonds, defined by vectors  $\mathbf{a}_1$  to  $\mathbf{a}_6$  that connect the sites within the unit cell, and six external bonds, defined by vectors  $\mathbf{a}'_1$  to  $\mathbf{a}'_6$  that connect sites of a given unit cell to sites of nearest-neighbor unit cells. The triangular faces of lattice tetrahedra lie in four sets of parallel planes and form kagome lattices in each. One of the four sets has its layer normal parallel to the  $(1, 1, 1)$ -direction. In the GPL, this latter set of planes will play a distinguished role, and we will refer to it as the GKL planes.

We generalize the pyrochlore lattice by allowing the basis sites to deviate from their original reference positions. In the undeformed pyrochlore lattice, there are 6 sets of straight filaments, built from the bonds on the 6 edges of the tetrahedra, that carry SSSs. Following Ref. [3], our generalization is designed to convert specific straight filaments into “zigzagged” ones that do not carry SSSs. In the GPL, the positions of the basis sites are displaced relative to those of the reference lattice,  $\mathbf{r}_i \rightarrow \mathbf{r}_i + \delta\mathbf{r}_i(X)$ , where  $X$  is a shorthand for a set of 4 parameters,  $X = (x_1, x_2, x_3, z)$ . We set the deviations  $\delta\mathbf{r}_i(X)$  to be

$$\delta\mathbf{r}_1(X) = x_1\sqrt{3}\hat{\mathbf{e}}_1 - x_2\hat{\mathbf{a}}_3, \quad (1a)$$

$$\delta\mathbf{r}_2(X) = x_2\sqrt{3}\hat{\mathbf{e}}_2 - x_3\hat{\mathbf{a}}_1, \quad (1b)$$

$$\delta\mathbf{r}_3(X) = x_3\sqrt{3}\hat{\mathbf{e}}_3 - x_1\hat{\mathbf{a}}_2, \quad (1c)$$

$$\delta\mathbf{r}_4(X) = -z\hat{\mathbf{n}}, \quad (1d)$$

where  $\hat{\mathbf{a}}_j = \mathbf{a}_j/|\mathbf{a}_j|$  and  $\hat{\mathbf{e}}_j = (\mathbf{a}_j \times \hat{\mathbf{n}})/|\mathbf{a}_j \times \hat{\mathbf{n}}|$  with  $\hat{\mathbf{n}}$  the unit vector in the  $(1, 1, 1)$ -direction. If  $z \neq 0$  and  $x_1 = x_2 = x_3 = 0$ , there are three sets of straight and three sets of zigzagged filaments, the former lying in the GKL planes. Nonzero  $x_n$ ’s produce the same distortions of the kagome lattices in the GKL planes as those in Ref. 3 with each  $x_n$  converting the straight filament parallel to  $\hat{\mathbf{a}}_n$  to a zigzag one. We have also studied more general versions of our model lattice in which sites 1 to 3

can adopt positions outside the GKL planes, thereby destroying their independent SSSs. For simplicity, however, we will focus on the model lattices described by Eq. (1). More specifically, we will focus on the 2 lattice conformations corresponding to the parameter settings  $X = X_1 \equiv (0.1, 0.1, 0.1, 0.1)$  and  $X = X_{-1} \equiv (-0.1, 0.1, 0.1, 0.1)$ , see Fig. 1. The GKL planes of these lattices are equivalent to the GKL conformations depicted in Fig. 2 (c) and (e) of Ref. [3], respectively.

Any central-force elastic network consisting of periodically repeated unit cells with  $n$  sites and  $n_B$  bonds is governed by the generalized Calladine-Maxwell theorem [1, 23, 24]  $n_0(\mathbf{q}) - s(\mathbf{q}) = dn - n_B$  at each wavevector  $\mathbf{q}$  in the BZ. It relates the number  $n_0(\mathbf{q})$  of zero modes, whose displacements do not stretch bonds, and the number  $s(\mathbf{q})$  of SSSs, in which bonds under tension exert no net forces on sites, to the invariant properties  $n$  and  $n_B$  of the unit cell. This important relation follows from the properties of the  $n_B \times dn$  compatibility matrix  $\mathbf{C}(\mathbf{q})$  relating bond displacements  $\mathbf{u}(\mathbf{q})$  to bond extensions  $\mathbf{e}(\mathbf{q})$  via  $\mathbf{C}(\mathbf{q})\mathbf{u}(\mathbf{q}) = \mathbf{e}(\mathbf{q})$  and the  $dn \times n_B$  equilibrium matrix  $\mathbf{Q}(\mathbf{q}) = \mathbf{C}^\dagger(\mathbf{q})$  relating bond tensions  $\mathbf{t}(\mathbf{q})$  to site forces  $\mathbf{f}(\mathbf{q})$  via  $\mathbf{Q}(\mathbf{q})\mathbf{t}(\mathbf{q}) = \mathbf{f}(\mathbf{q})$ . Zero modes constitute the null space of  $\mathbf{C}(\mathbf{q})$  and SSSs the null space of  $\mathbf{Q}(\mathbf{q})$ . When all masses and spring constants are set to unity, as we do here, the dynamical matrix governing the phonon spectrum is simply  $\mathbf{D}(\mathbf{q}) = \mathbf{Q}(\mathbf{q})\mathbf{C}(\mathbf{q})$ . Under periodic boundary conditions, the GPL satisfies  $dn = n_B$ , i.e., it is a Maxwell lattice [1] in which at each  $\mathbf{q}$  including  $\mathbf{q} = 0$ , there is always one SSS for each zero mode. The compatibility, equilibrium, and dynamical matrixes are all  $12 \times 12$  matrixes (see the supplemental material for details).

The elastic energy density can be expressed [30] in terms of the six-dimensional vector of symmetric strains  $\mathbf{U} = (u_{xx}, u_{yy}, u_{zz}, u_{xy}, u_{xz}, u_{yz})$  and the  $6 \times 6$  Voigt matrix  $\mathbf{K}$ :  $f = \frac{1}{2}\mathbf{U}^T \cdot \mathbf{K} \cdot \mathbf{U}$ . We calculate the  $\mathbf{K}$  of the GPLs from the normalized eigenvectors of the null space of  $\mathbf{Q}(\mathbf{q} = 0)$  [1]. The original pyrochlore lattice has  $s(\mathbf{q}) = 6$  corresponding to its six sets of straight filaments. This provides a sufficient number of SSSs at  $\mathbf{q} = 0$  to stabilize all six independent strains. For  $X_1$  and  $X_{-1}$ , there are no straight filaments in the lattice, but  $s(\mathbf{q} = 0) = 3$  because there are  $n_0(\mathbf{q} = 0) = 3$  zero modes corresponding to the rigid translations of the lattice. Thus,  $\mathbf{K}$  has three zero and three positive eigenvalues for these lattice conformations. The former imply the existence of three independent macroscopic deformations free of restoring forces – the Guest modes [31]  $\mathbf{U}^G$  of the lattice. For  $X_1$ , the three Guest modes are proportional to  $(2, 0, 0, 0, 0, -1)$ ,  $(0, 2, 0, 0, -1, 0)$  or  $(0, 0, 2, -1, 0, 0)$ . Internally, these deformations are realized by rigid rotations of the constituent tetrahedra, about  $\hat{\mathbf{n}}$ , that change no bond lengths. For  $X_{-1}$ , the Guest modes involve all components of  $\mathbf{U}$ .

The topological properties of the phononic band struc-

ture of the GPL are determined by the  $\mathbf{C}$  or  $\mathbf{Q}$  matrixes [3]. The determinants of these matrices map a path in  $\mathbf{q}$ -space onto a path in the complex plane. Because  $\mathbf{Q}$  and  $\mathbf{C}$  are invariant under  $\mathbf{q} \rightarrow \mathbf{q} + \mathbf{G}$  for any reciprocal lattice vector  $\mathbf{G}$ , any path in  $\mathbf{q}$ -space whose start and end points are separated by a reciprocal lattice vector will map onto a closed path in the complex plane. For simplicity, we focus on paths in  $\mathbf{q}$ -space that are straight lines along the primitive vectors  $\mathbf{b}_1, \mathbf{b}_2, \mathbf{b}_3$ , satisfying  $\mathbf{b}_i \cdot \mathbf{T}_j = 2\pi\delta_{ij}$ , of the reciprocal lattice. The integer winding numbers of the corresponding closed paths in the complex plane are

$$m(\mathbf{q}_\perp, \mathbf{G}) = \frac{1}{2\pi i} \int_0^G dp \frac{d}{dp} \text{LogDet } \mathbf{Q}(\mathbf{q}_\perp, p, \mathbf{G}), \quad (2)$$

where  $\mathbf{q}_\perp$  specifies the components of  $\mathbf{q}$  in the surface BZ of the lattice plane defined by  $\mathbf{G}$ ,  $p$  is the component of  $\mathbf{q}$  along  $\mathbf{G}$ , and  $G = |\mathbf{G}|$ . In fully gapped systems, the winding numbers are independent of  $\mathbf{q}_\perp$ . In systems with Weyl singularities, they are not. We will utilize this fact in the following to detect and map out Weyl singularities in the GPL. The idea is to calculate the winding numbers for an entire set of  $\mathbf{q}_\perp$ 's in a given surface BZ. For example, for our integration along  $\mathbf{b}_1$ , we sweep the BZ that is spanned by the unit vectors  $\hat{\mathbf{c}}_{1,1} = (\mathbf{b}_1 \times \mathbf{b}_2)/|\mathbf{b}_1 \times \mathbf{b}_2|$  and  $\hat{\mathbf{c}}_{1,2} = (\mathbf{b}_1 \times \hat{\mathbf{c}}_{1,1})/|\mathbf{b}_1 \times \hat{\mathbf{c}}_{1,1}|$ . Figure 2 compiles our results for the winding numbers  $m_i(\mathbf{q}_\perp) \equiv m(\mathbf{q}_\perp, \mathbf{G} = \mathbf{b}_i)$ . There is a qualitative difference between  $X_{+1}$  and  $X_{-1}$  in the values and distribution of their winding numbers: For  $X_1$ ,  $m_i = -1$  throughout the surface BZ associated with each  $\mathbf{b}_i$ . For  $X_{-1}$ , boundaries determined by the projections of Weyl lines onto any given surface BZ divide the latter into regions with different winding numbers. In addition to the Weyl lines, for both  $X_1$  and  $X_{-1}$  there is a two-fold degenerate line of zero modes along the  $(1, 1, 1)$ -direction (that we verify by diagonalizing  $\mathbf{D}$  for  $\mathbf{q}$  along  $\hat{\mathbf{n}}$ ) whose winding number is zero. This line is a consequence of the  $\mathbf{q}_\perp = 0$  SSS of the flat GKL planes in the GPL. In the more general version of our model lattice, alluded to above, this line splits up into two oppositely-charged Weyl lines when the reference positions of one of the basis sites 1, 2 or 3 is moved out of the GKL plane. These Weyl lines are separated by a distance proportional to the distance of the respective sites from the GKL plane.

We can reconstruct the Weyl lines in 3d from their projections onto the 2d BZ defined by the  $\mathbf{b}_i$ 's shown in Fig 2. To this end, we use the following approach: A point on a projected line with coordinates  $(q_1, q_2)$  in the plane perpendicular to  $\mathbf{b}_1$  is replaced by  $\mathbf{q} = p\hat{\mathbf{b}}_1 + q_1\hat{\mathbf{c}}_{1,1} + q_2\hat{\mathbf{c}}_{1,2}$ , where  $\hat{\mathbf{b}}_1 = \mathbf{b}_1/|\mathbf{b}_1|$ , and likewise for the projection onto the plane perpendicular to  $\mathbf{b}_2$ . Then, we calculate the intersections of the resulting manifolds. Finally, we discard all intersection points whose projections onto the plane perpendicular to  $\mathbf{b}_3$  are incompatible with our results for

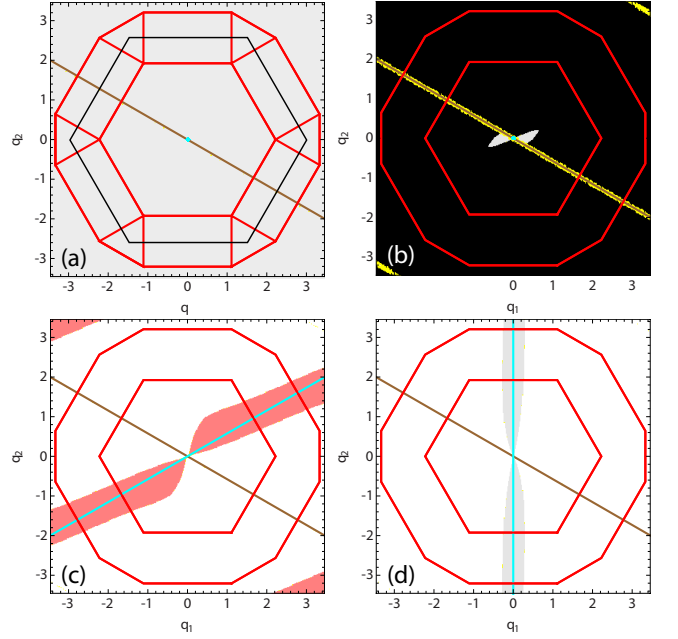


FIG. 2. (Color Online) Winding numbers  $m_1, m_2$  and  $m_3$  for (a)  $X_1$  and (b,c,d)  $X_{-1}$ .  $q_1$  and  $q_2$  are the components of the respective  $\mathbf{q}_\perp$ s. The (red) polygons depict projections of the edges of the top and equatorial surfaces of the BZ onto these planes. The black polygon in (a) represents the surface BZ. The color-coding of the shaded areas is as follows: pink corresponds to winding number 1, white to 0, gray to -1, and black to -2. Yellow indicates points where the numerical integration failed to converge properly. The (brown) solid lines indicate the 2-fold degenerate zero mode along the  $(1, 1, 1)$ -direction. The (cyan) light line indicates the  $(1, 1, -1)$ -direction and is a guide to the eye.

$m_3$ . Our results obtained in this way for the Weyl lines in 3d are depicted in Fig. 3. As follows from the previous paragraph, the only zero modes that we encounter for  $X_1$  lie on a line along  $\hat{\mathbf{n}}$ . For  $X_{-1}$  there is in addition a pair of Weyl lines. These Weyl lines do not form closed loops but follow a path in the BZ between points separated by a reciprocal lattice vector.

It is informative to compare our numerical results to analytical predictions for the Weyl lines. To this end, we consider small deviations about the original pyrochlore lattice as parameterized by  $X_\varepsilon \equiv (\varepsilon, \varepsilon, \varepsilon)$  and  $X_{-\varepsilon} \equiv (-\varepsilon, \varepsilon, \varepsilon)$ , and we expand  $\det \mathbf{C}(\mathbf{q})$  in powers of the  $q_i$  and  $\varepsilon$ . For both  $X_\varepsilon$  and  $X_{-\varepsilon}$ , the resulting expansion is of the form

$$\det \mathbf{C} = f^{(3)}(\mathbf{q}) \varepsilon^3 + f^{(4)}(\mathbf{q}) \varepsilon^2 + f^{(5)}(\mathbf{q}) \varepsilon + O(q_i^6), \quad (3)$$

where the  $f^{(m)}(\mathbf{q})$  are different functions of  $m$ th order in  $q_i$  for  $X_\varepsilon$  and  $X_{-\varepsilon}$  that vanish for any  $\mathbf{q}$  along  $\hat{\mathbf{n}}$ . We solve for the wave-vectors that are zeros of the right hand side of Eq. (3). For  $X_\varepsilon$ , there is only one real solution that corresponds to any  $\mathbf{q}$  along  $\hat{\mathbf{n}}$ . For  $X_{-\varepsilon}$ , on the other hand, there are additional real solutions, which we

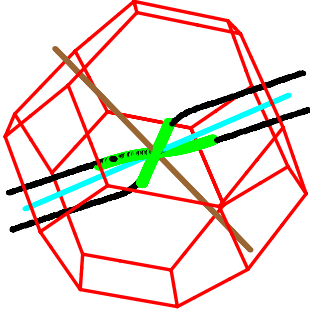


FIG. 3. (Color Online) Weyl lines for  $X_{-1}$  traversing the (red) dedecahedron-shaped BZ. The (black) points mark our numerical reconstruction of the Weyl lines, the (green) lines stem from our analytical estimate based on the expansion of  $\det \mathbf{C}$ , Eq. (3). For  $X_1$ , only the two-fold degenerate (brown) line along the  $(1, 1, 1)$ -direction is present.

display for  $\varepsilon = 0.1$  in Fig. 3. Note the nice agreement at small  $q$  between the numerical and analytical results for  $X_1$  and  $X_{-1}$ .

Now, we turn to surface modes. In general, the total edge index  $\nu(\mathbf{q}_\perp, \mathbf{G}) = n_0(\mathbf{q}_\perp, \mathbf{G}) - s(\mathbf{q}_\perp, \mathbf{G})$  is the sum of a local part  $\nu_L(\mathbf{G})$  [1, 3], which is independent of  $\mathbf{q}_\perp$ , and a topological part  $\nu_T(\mathbf{q}_\perp, \mathbf{G})$ . At free surfaces,  $s(\mathbf{q}_\perp, \mathbf{G}) = 0$ , and  $\nu(\mathbf{q}_\perp, \mathbf{G}) = n_0(\mathbf{q}_\perp, \mathbf{G})$ . The local count is  $\mathbf{G} \cdot \mathbf{R}_L / (2\pi)$ , where  $\mathbf{G}$  is the *outer* normal to its lattice plane and  $\mathbf{R}_L$  is the difference between the dipole moment of the surface unit cell and that of the reference cell of Fig. 1 (See supplementary material). In systems without Weyl singularities, the winding numbers  $m_i$  are independent of wave vector as mentioned above and define a topological charge  $\mathbf{R}_T = \sum_i m_i \mathbf{T}_i$ . For  $X_1$ , in particular,  $\mathbf{R}_T = -(2, 2, 2)$ . The topological surface count in these systems is simply  $\nu_T(\mathbf{G}) = \mathbf{G} \cdot \mathbf{R}_T / (2\pi)$ , independent of  $\mathbf{q}_\perp$ . In systems with Weyl points the topological count  $\nu_T(\mathbf{q}_\perp, \mathbf{G}) = m(\mathbf{q}_\perp, \mathbf{G})$  depends on  $\mathbf{q}_\perp$  and is not defined globally.

For simplicity, we focus here on surfaces whose normals are parallel to primitive vectors  $\mathbf{b}_i$  of the reciprocal lattice. We calculate the complex inverse penetrations depths  $\kappa(\mathbf{q}_\perp)$  by setting  $\mathbf{q} = i\kappa\mathbf{b}_1 + q_1\hat{\mathbf{c}}_{1,1} + q_2\hat{\mathbf{c}}_{1,2}$ , and similarly for  $i = 2, 3$ , and solving for the roots of  $\det \mathbf{C}(i\kappa, q_1, q_2) = 0$ . Positive values of  $\kappa' \equiv \text{Re}(\kappa)$  correspond to zero modes that decay in the direction of  $\mathbf{b}_1$  and that are, therefore, localized on the surface with outer normal along  $-\mathbf{b}_1$ . Negative values of  $\kappa'$  correspond to states localized on the opposite surface with outer normal  $\mathbf{b}_1$ . Figure 4 presents plots of  $\kappa'$  and  $\nu_{T,i} = \nu_T(-\mathbf{b}_i)$  as a function of  $q_1$  and fixed  $q_2 = 0.1$  for our three surface orientations and for  $X_1$  and  $X_{-1}$ . For each  $X$  and  $\mathbf{b}_i$ , there are positive and negative values of  $\kappa'$  indicating localization on both surfaces, but as required by the Calladine-Maxwell theorem, there is always a total of three zero modes on the two surfaces. For  $X_1$ , the three  $\kappa'$ s are the same function of  $q_1$  for all  $\mathbf{b}_i$ s. In addition  $\nu_{T,i} = 1.0$  is

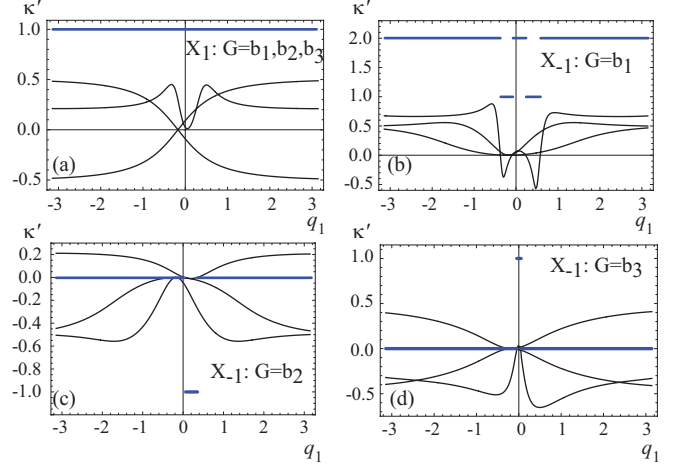


FIG. 4. (Color Online)  $\kappa'$  (black lines) and  $\nu_T$  (blue straight lines) of surface zero modes with fixed  $q_2 = 0.1$  for (a)  $X_1$  and (b, c, d)  $X_{-1}$ .

independent of  $i$ . This implies that  $\nu_{L,i} = \nu_L(-\mathbf{b}_i) = 1.0$  for every  $i$ .  $\nu_L$  is a property of a surface that does not change if the topological class is varied by changing  $X$ . For  $X_{-1}$ , the functions  $\kappa'(q_1)$  are different for the different surfaces, and the number of positive and negative values undergo discontinuous changes in accord with similar changes in  $\nu_{T,i}(q_1)$ . At the  $-\mathbf{b}_1$  surface,  $\nu_{T1}$  takes on values of 2 and 1, and, as required, the number of modes localized on the  $-\mathbf{b}_1$  surface changes from 2 to 1 and back again with the jumps in  $\nu_{T1}$ . Similarly, for  $-\mathbf{b}_2$  surface,  $\nu_{T2}$  takes on values 0 and  $-1$  and  $n_0(q_1, -\mathbf{b}_2)$  values 1 and 0 (though the latter region is relatively small); and for the  $-\mathbf{b}_3$  surface,  $\nu_{T3}$  is zero almost everywhere except for a very small region near the origin where it is equal to 1 and  $\nu_3(q_1, -\mathbf{b}_3)$  is either 1 or 0. In the supplementary material, we provide more detail about the calculation of  $\mathbf{R}_L$ , and we show results for surfaces perpendicular to the  $\mathbf{G} = \pm 2\pi(1, 0, 0)$  reciprocal lattice vector. In this case, four bonds must be cut to liberate a strip, and there are four surface zero modes distributed between the two surfaces.

In conclusion, we have studied topological phonons in 3d in a generalized pyrochlore lattice. Our model lattice displays distinct topological states, in the form of Weyl lines that traverse the Brillouin Zone, and thereby underscores the validity in 3d of the general theory for topological phonons laid out in Ref. [3]. Together with the recent work on generalized square lattices [16] and 2d models of jammed matter [17], our work hints that Weyl singularities are a common feature in Maxwell lattices and that the GKL is special in that its unit cell does not provide enough degrees of freedom to have them. The present work indicates that the GPL is a candidate for detecting Weyl lines in mechanical experiments. Given the advancement of 3d printing technology, the creation



of a GPL-like meta-material in a lab should be within reach in the foreseeable future.

This work was supported by the NSF under No. DMR-1104701 (OS, TCL), No. DMR-1120901 (OS, TCL). CLK was supported by a Simons Investigators Grant and TCL by a Simons Fellows grant.

- 
- [1] T. C. Lubensky, C. L. Kane, X. Mao, A. Souslov, and K. Sun, Reports on progress in physics. Physical Society (Great Britain) **78**, 073901 (2015).
  - [2] K. Sun, A. Souslov, X. Mao, and T. C. Lubensky, PNAS **109**, 12369 (2012).
  - [3] C. Kane and T. C. Lubensky, Nature Phys. **10**, 39 (2014).
  - [4] W. P. Su, J. R. Schrieffer, and A. J. Heeger, Phys. Rev. Lett. **42**, 1698 (1979).
  - [5] B. I. Halperin, Phys. Rev. B **25**, 2185 (1982).
  - [6] F. D. M. Haldane, Phys. Rev. Lett. **61**, 2015 (1988).
  - [7] C. L. Kane and E. J. Mele, Phys. Rev. Lett. **95**, 146802 (2005).
  - [8] B. A. Bernevig, T. L. Hughes, and S.-C. Zhang, Science **314**, 1757 (2006).
  - [9] J. E. Moore and L. Balents, Phys. Rev. B **75**, 121306 (2007).
  - [10] L. Fu, C. L. Kane, and E. J. Mele, Phys. Rev. Lett. **98**, 106803 (2007).
  - [11] Z. Hasan and C. Kane, Rev. Mod. Phys. **82**, 3045 (2010).
  - [12] X.-L. Qi and S.-C. Zhang, Rev. Mod. Phys. **83**, 1057 (2011).
  - [13] B. G. Chen, N. Upadhyaya, and V. Vitelli, Proc. Natl. Acad. Sci. USA **111**, 13004 (2014).
  - [14] J. Paulose, B. G. Chen, and V. Vitelli, Nature Physics **11**, 153 (2015).
  - [15] J. Paulose, A. S. Meeussen, and V. Vitelli, Proc. Natl. Acad. Sci. USA **112**, 7639 (2015).
  - [16] D. Z. Rocklin, B. G.-g. Chen, M. Falk, V. Vitelli, and T. Lubensky, Phys. Rev. Lett. **116**, 135503 (2016).
  - [17] D. Sussman, O. Stenull, and T. Lubensky, unpublished (2016).
  - [18] G. Volovik, Lecture Notes in Physics **718**, 3173 (2007).
  - [19] A. A. Burkov, M. D. Hook, and L. Balents, Phys. Rev. B **84**, 235126 (2011).
  - [20] Y. Kim, B. J. Wieder, C. L. Kane, and A. M. Rappe, Phys. Rev. Lett. **115**, 036806 (2015).
  - [21] R. Yu, H. M. Weng, Z. Fang, X. Dai, and X. Hu, Phys. Rev. Lett. **115**, 036807 (2015).
  - [22] L. Lu, L. Fu, J. D. Joannopoulos, and M. Soljacic, Nature Photonics **7**, 294 (2013).
  - [23] J. C. Maxwell, Philos. Mag. **27**, 294 (1864).
  - [24] C. R. Calladine, Int. J. Solids Struct. **14**, 161 (1978).
  - [25] X. G. Wan, A. M. Turner, A. Vishwanath, and S. Y. Savrasov, Phys. Rev. B **83**, 205101 (2011).
  - [26] S.-Y. Xu, I. Belopolski, A. Nasser, M. Neupane, G. Bian, C. Zhang, R. Sankar, G. Chang, Z. Yuan, C.-C. Lee, S.-M. Huang, H. Zheng, J. Ma, D. S. Sanchez, B. Wang, A. Bansil, F. Chou, P. P. Shibayev, H. Lin, S. Jia, and M. Z. Hasan, Science **249**, 613 (2015).
  - [27] D. P. Divincenzo and E. J. Mele, Physical Review B **29**, 1685 (1984).
  - [28] A. H. Castro Neto, F. Guinea, N. M. R. Peres, K. S. Novoselov, and A. K. Geim, Reviews of Modern Physics **81**, 109 (2009).
  - [29] S. M. Young and C. L. Kane, Physical Review Letters **115**, 126803 (2015).
  - [30] C. Kittel, *Introduction to Solid State Physics*, 4th ed. (John Wiley and Sons, New York, 1971).
  - [31] S. D. Guest and J. W. Hutchinson, J. Mech. Phys. Solids **51**, 383 (2003).

## SUPPLEMENTAL MATERIAL

### Equilibrium matrix

In terms of the primitive translation vectors, the position of the origin (site 4) of a unit cell I can be la-

$$\mathbf{Q}(\mathbf{q}) = \begin{pmatrix} -\hat{a}_{1,1} & 0 & \hat{a}_{3,1} & \hat{a}_{4,1} & 0 & 0 & \hat{a}'_{1,1}e^{-i\mathbf{q}\cdot\boldsymbol{\tau}_1} & 0 & -\hat{a}'_{3,1} & -\hat{a}'_{4,1} & 0 & 0 \\ -\hat{a}_{1,2} & 0 & \hat{a}_{3,2} & \hat{a}_{4,2} & 0 & 0 & \hat{a}'_{1,2}e^{-i\mathbf{q}\cdot\boldsymbol{\tau}_1} & 0 & -\hat{a}'_{3,2} & -\hat{a}'_{4,2} & 0 & 0 \\ -\hat{a}_{1,3} & 0 & \hat{a}_{3,3} & \hat{a}_{4,3} & 0 & 0 & \hat{a}'_{1,3}e^{-i\mathbf{q}\cdot\boldsymbol{\tau}_1} & 0 & -\hat{a}'_{3,3} & -\hat{a}'_{4,3} & 0 & 0 \\ \hat{a}_{1,1} & -\hat{a}_{2,1} & 0 & 0 & \hat{a}_{5,1} & 0 & -\hat{a}'_{1,1} & \hat{a}'_{2,1}e^{-i\mathbf{q}\cdot\boldsymbol{\tau}_2} & 0 & 0 & -\hat{a}'_{5,1} & 0 \\ \hat{a}_{1,2} & -\hat{a}_{2,2} & 0 & 0 & \hat{a}_{5,2} & 0 & -\hat{a}'_{1,2} & \hat{a}'_{2,2}e^{-i\mathbf{q}\cdot\boldsymbol{\tau}_2} & 0 & 0 & -\hat{a}'_{5,2} & 0 \\ \hat{a}_{1,3} & -\hat{a}_{2,3} & 0 & 0 & \hat{a}_{5,3} & 0 & -\hat{a}'_{1,3} & \hat{a}'_{2,3}e^{-i\mathbf{q}\cdot\boldsymbol{\tau}_2} & 0 & 0 & -\hat{a}'_{5,3} & 0 \\ 0 & \hat{a}_{2,1} & -\hat{a}_{3,1} & 0 & 0 & \hat{a}_{6,1} & 0 & -\hat{a}'_{2,1} & \hat{a}'_{3,1}e^{-i\mathbf{q}\cdot\boldsymbol{\tau}_3} & 0 & 0 & -\hat{a}'_{6,1} \\ 0 & \hat{a}_{2,2} & -\hat{a}_{3,2} & 0 & 0 & \hat{a}_{6,2} & 0 & -\hat{a}'_{2,2} & \hat{a}'_{3,2}e^{-i\mathbf{q}\cdot\boldsymbol{\tau}_3} & 0 & 0 & -\hat{a}'_{6,2} \\ 0 & \hat{a}_{2,3} & -\hat{a}_{3,3} & 0 & 0 & \hat{a}_{6,3} & 0 & -\hat{a}'_{2,3} & \hat{a}'_{3,3}e^{-i\mathbf{q}\cdot\boldsymbol{\tau}_3} & 0 & 0 & -\hat{a}'_{6,3} \\ 0 & 0 & 0 & -\hat{a}_{4,1} & -\hat{a}_{5,1} & -\hat{a}_{6,1} & 0 & 0 & 0 & \hat{a}'_{4,1}e^{-i\mathbf{q}\cdot\boldsymbol{\tau}_4} & \hat{a}'_{5,1}e^{-i\mathbf{q}\cdot\boldsymbol{\tau}_5} & \hat{a}'_{6,1}e^{i\mathbf{q}\cdot\boldsymbol{\tau}_6} \\ 0 & 0 & 0 & -\hat{a}_{4,2} & -\hat{a}_{5,2} & -\hat{a}_{6,2} & 0 & 0 & 0 & \hat{a}'_{4,2}e^{-i\mathbf{q}\cdot\boldsymbol{\tau}_4} & \hat{a}'_{5,2}e^{-i\mathbf{q}\cdot\boldsymbol{\tau}_5} & \hat{a}'_{6,2}e^{i\mathbf{q}\cdot\boldsymbol{\tau}_6} \\ 0 & 0 & 0 & -\hat{a}_{4,3} & -\hat{a}_{5,3} & -\hat{a}_{6,3} & 0 & 0 & 0 & \hat{a}'_{4,3}e^{-i\mathbf{q}\cdot\boldsymbol{\tau}_4} & \hat{a}'_{5,3}e^{-i\mathbf{q}\cdot\boldsymbol{\tau}_5} & \hat{a}'_{6,3}e^{i\mathbf{q}\cdot\boldsymbol{\tau}_6} \end{pmatrix}$$

where the  $\hat{a}$ 's and  $\hat{a}'$ 's here are the normalized interior and exterior bond vectors of the generalized lattice.

### Surface with $\mathbf{G} = \mathbf{b}_1$ – unit cell and local count

Here, we provide some additional information about the calculation of the surface zero modes for surfaces with normals along the primitive reciprocal lattice vector  $\mathbf{G} = \pm\mathbf{b}_1$ . As shown in Fig. 5, we have to cut 3 bonds (1', 3, 4 in the figure) per surface unit cell to liberate a slab with periodic boundary conditions perpendicular to  $\mathbf{G}$  and opposite surfaces parallel to the plane defined by the (blue) quadrilateral. At the lower surface with  $\mathbf{b}_1$  the *inner* normal, the exterior bond 1 protrudes, and at the upper surface with  $\mathbf{b}_1$  the *outer* normal, bonds 3 and 4 protrude. Note that the lower surface in this case is essentially flat whereas the upper one has periodically spaced upward pointing tetrahedra. To convert the reference unit cell to one compatible with the lower surface with  $\mathbf{G} = -\mathbf{b}_1 = \pi(-1, -1, 1)$ , we have only to move exterior bond 1 by the vector  $\mathbf{T}_b = -(\mathbf{a}_1 + \mathbf{a}'_1) = \mathbf{T}_1 - \mathbf{T}_2 = (1, 0, -1)$ , which implies that  $\mathbf{R}_L^{\text{lower}} = 3\sum_s \Delta\mathbf{r}_s - \sum_b \Delta\mathbf{r}_b = -\mathbf{T}_1 + \mathbf{T}_2$ , where  $\Delta\mathbf{r}_s$  and  $\Delta\mathbf{r}_b$  are, respectively, the displacement of sites and bonds from the reference unit cell to the surface compatible one. Thus  $\nu_L^{\text{lower}} = (-\mathbf{b}_1/(2\pi)) \cdot \mathbf{R}_L^{\text{lower}} = 1$ . To convert the reference unit cell to one compatible with the upper surface, the protruding outer bonds 3 and 4 must be displaced by  $\mathbf{T}_3 - \mathbf{T}_1$  and  $-\mathbf{T}_1$ , respectively, yielding  $\mathbf{R}_L^{\text{upper}} = 2\mathbf{T}_1 - \mathbf{T}_3$  and  $\nu_L^{\text{upper}} = \mathbf{b}_1 \cdot \mathbf{R}_L^{\text{upper}}/2\pi = 2$ .

beled by 3 integers  $l_1, l_2$ , and  $l_3$ ,  $\mathbf{T}(l_1, l_2, l_3) = l_1\mathbf{T}_1 + l_2\mathbf{T}_2 + l_3\mathbf{T}_3$ . Using the abbreviations  $\boldsymbol{\tau}_1 = \mathbf{T}(-1, 1, 0)$ ,  $\boldsymbol{\tau}_2 = \mathbf{T}(0, -1, 1)$ ,  $\boldsymbol{\tau}_3 = \mathbf{T}(1, 0, -1)$ ,  $\boldsymbol{\tau}_4 = \mathbf{T}(1, 0, 0)$ ,  $\boldsymbol{\tau}_5 = \mathbf{T}(0, 1, 0)$  and  $\boldsymbol{\tau}_6 = \mathbf{T}(0, 0, 1)$ , the equilibrium matrix of our model lattice in  $\mathbf{q}$ -space reads

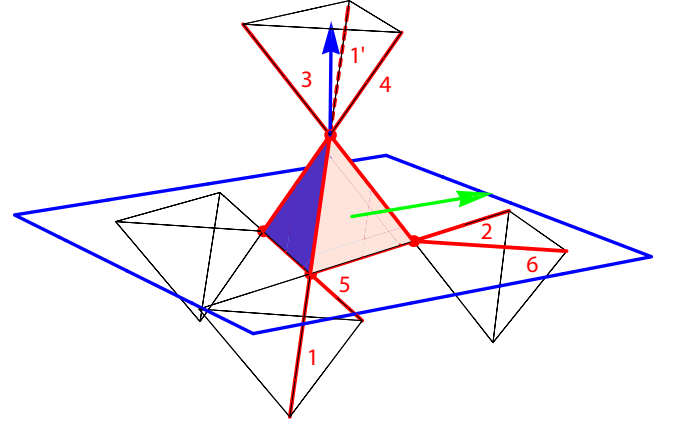


FIG. 5. (Color Online) Our unit cell and a surface with inward normal along  $\mathbf{b}_1$ . The rectangular (blue) frame indicates the surface to be liberated and the upward (blue) arrow its normal. The numbered red lines symbolize the exterior bonds of the unit cell.

The topological polarization for the  $X_1$  lattice is  $\mathbf{R}_T = -(2, 2, 2)$ , so that  $\nu_T^{\text{lower}} = -\mathbf{b}_1 \cdot \mathbf{R}_T = 1$  and  $\mathbf{R}_T^{\text{upper}} = -1$ . Thus,  $\nu_L^{\text{lower}} = \nu_L^{\text{lower}} + \nu_T^{\text{lower}} = n_0(-\mathbf{b}_1) = 1 + 1 = 2$  and  $\nu_T^{\text{upper}} = n_0(\mathbf{b}_1) = 2 - 1 = 1$  in agreement with Fig. (4).

### Surface with $\mathbf{G} \parallel (1, 0, 0)$

To liberate a slab with surfaces perpendicular to  $\mathbf{G}_x = 2\pi(1, 0, 0) = \mathbf{b}_1 + \mathbf{b}_3$ , we need to cut the four exterior

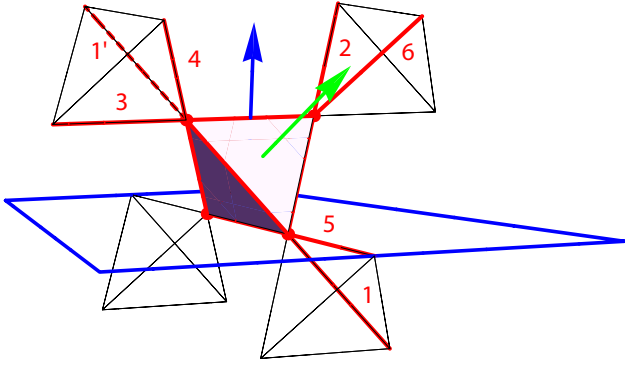


FIG. 6. (Color Online) Our unit cell and a surface with inward normal along  $(1, 0, 0)$ . The color-coding is as in Fig. 5.

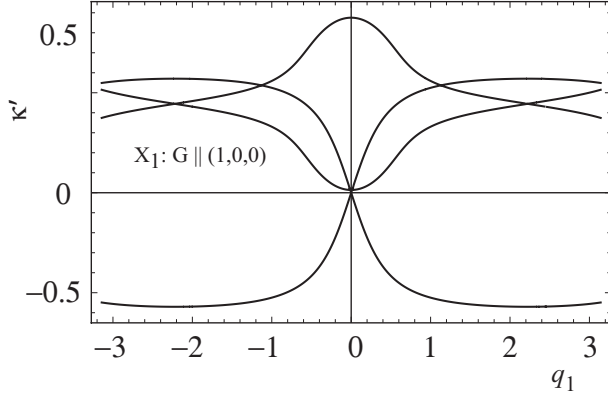


FIG. 7. (Color Online)  $\kappa'$  of surface zero modes for  $\mathbf{G} = 2\pi(1, 0, 0)$  and fixed  $q_2 = 0.1$  for  $X_1$ .

bonds 1', 2, 4, and 6 in Fig. 7, and we expect total of 4 zero modes as the displayed in Fig. 7. To convert the reference cell to one compatible with the lower surface with  $\mathbf{G}^{\text{lower}} = -\mathbf{G}_x$ , we need, as in the previous example, displace only exterior bond 1, so that  $\mathbf{R}_L^{\text{lower}} = (-1, 0, 1)$  to produce  $\nu_L^{\text{lower}} = -\mathbf{G}_x \cdot \mathbf{R}_L^{\text{lower}} / 2\pi = 2$ . To create a cell compatible with the upper surface, we need to displace exterior bond 2 by  $-(\mathbf{a}_2 + \mathbf{a}_2') = -\mathbf{T}_3 + \mathbf{T}_2$ , bond 4 by  $-\mathbf{T}_1$ , and bond 6 by  $-\mathbf{T}_3$ . These moves yield  $\mathbf{R}_L^{\text{upper}} = 2\mathbf{T}_3 - \mathbf{T}_2 + \mathbf{T}_1$  and  $\nu_T^{\text{upper}} = 3$ , and  $\nu^{\text{upper}} = n_0(\mathbf{G}_x) = 3 - 2 = 1$  in agreement with the three decaying modes (lower surface) and one growing mode (upper surface) of Fig. 7. Similar analyses can be applied to the  $X_1$  and other lattices and to other surfaces and domain walls.